



Cite this: *J. Mater. Chem. A*, 2022, 10, 3226

## Enhanced ion transport behaviors in composite polymer electrolyte: the case of a looser chain folding structure†

Dexuan Pei,<sup>a</sup> Rui Ma,<sup>\*a</sup> Gang Yang,<sup>a</sup> Yuhang Li,<sup>a</sup> Can Huang,<sup>a</sup> Ziyang Liu,<sup>a</sup> Shuo Huang,<sup>a</sup> Guozhong Cao <sup>b</sup> and Hongyun Jin <sup>\*a</sup>

All-solid-state batteries based on composite polymer electrolytes (CPEs) have attracted significant attention due to their high energy density, security and flexibility. Usually, the enhanced electrochemical performance of CPEs is attributed to the reduction in crystallinity in the polymer matrix by introducing inorganic fillers. However, studies on the effects of the change in the chain folding structure in polymers on the ion transport behaviors after the addition of fillers are limited. In this work, we fabricated CPEs with different-size inorganic Al<sub>2</sub>O<sub>3</sub> nanofillers. The results showed that CPEs with smaller-size Al<sub>2</sub>O<sub>3</sub> nanoparticles exhibited shorter  $T_1$  and longer  $T_2$  relaxation times, implying the looser chain folding structure in these CPEs. Particularly, the CPEs with 30 nm-sized Al<sub>2</sub>O<sub>3</sub> particles exhibited good conductivity of  $4.87 \times 10^{-5}$  S cm<sup>-1</sup> and high Li<sup>+</sup> transference number of 0.65. We conclude that the looser chain folding structure in the polymer matrix, which provides more channels for Li<sup>+</sup> transport, plays a major role in improving the electrochemical properties of the electrolyte with an excellent capacity retention of 81.3% after 500 cycles at 1.0C in LFP/CPE/Li batteries. This provides novel insight to clarify the mechanism of the chain folding structure and how it influences the lithium ion transport, thus improving the electrochemical performances of CPEs.

Received 14th December 2021  
Accepted 3rd January 2022

DOI: 10.1039/d1ta10669d

rsc.li/materials-a

## Introduction

Lithium-ion batteries (LIBs) are widely used in portable electronic devices such as mobile phones, notebook computers, and even hybrid electric vehicles and electric vehicles.<sup>1,2</sup> However, LIBs often suffer from low energy density, electrolyte leakage, and potential safety hazards, which hinder their practical applications.<sup>3,4</sup> Accordingly, an ideal category to solve these issues is the use of solid-state electrolytes to replace traditional organic liquid electrolytes.<sup>5,6</sup> Composite polymer electrolytes (CPEs) have attracted significant attention given that they exhibit high mechanical strength and good flexibility, as well as lightweight nature and machinability. Thus, CPEs can effectively inhibit the growth of lithium dendrites and maintain good interface contact between the electrolyte and electrode.<sup>7</sup>

Since Parker and Armand reported that poly(ethylene oxide) (PEO)<sup>8,9</sup> together with lithium salts can transport lithium ions, several types of polymers such as polyacrylonitrile (PAN),<sup>10</sup> poly(methyl methacrylate),<sup>11</sup> and polyvinylidene fluoride

(PVDF)<sup>12</sup> were employed as the matrix of CPEs. However, their lithium ion conductivity ( $\sigma$ ) cannot reach  $10^{-4}$  S cm<sup>-1</sup>. Furthermore, the thermal stability and chemical stability of pure polymer solid electrolytes are poor, and their mechanical strength is not high. Accordingly, an efficient method to address these shortcomings of pure polymer electrolytes is the addition of inorganic fillers to the polymer matrix to prepare CPEs.<sup>13</sup> These inorganic fillers can be divided into active fillers and inert fillers. Active fillers usually include LATP, LLZO, and LAGP.<sup>14–16</sup> Zhang *et al.* reported that a CPE consisting of LLZO particles and PVDF-HFP polymer matrix exhibited an initial reversible discharge capacity of 120 mA h g<sup>-1</sup> at 0.5C and excellent cycling performance for 180 cycles at room temperature.<sup>17</sup> Chen *et al.* studied the Li ion conducting performance of a series of CPEs fabricated by incorporating LLZO into the PEO/LiTFSI matrix. The  $\sigma$  of CPEs was  $1.19 \times 10^{-4}$  S cm<sup>-1</sup> at room temperature and the all-solid-state Li//LFP cell assembled with this type of CPE delivered an initial discharge capacity of 130.2 mA h g<sup>-1</sup> and capacity retention of 80.0% after 500 cycles at 1.0C.<sup>18</sup> Alternatively, inert fillers usually include Al<sub>2</sub>O<sub>3</sub>,  $\gamma$ -LiAlO<sub>2</sub>, SiO<sub>2</sub> and TiO<sub>2</sub>. Yang *et al.* prepared  $\alpha$ -Al<sub>2</sub>O<sub>3</sub>-containing PAN-based CPEs with a conductivity of  $5.7 \times 10^{-4}$  S cm<sup>-1</sup> at room temperature.<sup>19</sup> Zhang *et al.* synthesized novel CPEs by introducing Al<sub>2</sub>O<sub>3</sub> nanowires into the polymer matrix and the  $\sigma$  of CPEs was  $2.66 \times 10^{-5}$  S cm<sup>-1</sup>.<sup>20</sup> CPEs showed a discharge capacity of 162 mA h g<sup>-1</sup> at 0.2, 0.5 and 1C, and an average

<sup>a</sup>Faculty of Materials Science and Chemistry, China University of Geosciences, Wuhan 430074, China. E-mail: jinhongyun@cug.edu.cn

<sup>b</sup>Department of Materials Science & Engineering, University of Washington, WA 98195, USA

† Electronic supplementary information (ESI) available. See DOI: 10.1039/d1ta10669d

discharge capacity of  $158 \text{ mA h g}^{-1}$  over 200 cycles. Thus, it is highly desirable to understand how these fillers affect or regulate the structure of the polymer matrix, and then act on the lithium ion transport behaviors.

The main effect of fillers is to weaken the intermolecular force of the polymer due to the isolation of steric hindrance, thereby increasing the mobility of the polymer chains and reducing their crystallinity, which provides the possibility of increasing the lithium ion transport ability. In the case of active fillers, they can also provide extra  $\text{Li}^+$ , and active fillers/polymer interfaces are considered as rapid  $\text{Li}^+$  transportation paths. Conversely, in the case of inert fillers, there is a Lewis acid–base pair interaction between the filler and anion group of the lithium salt, which is beneficial for dissolving the lithium salt and releasing more  $\text{Li}^+$ .<sup>21</sup> In summary, previous studies mainly focused on increasing the amorphous region in the polymer matrix to increase the  $\text{Li}^+$  transport in CPEs.<sup>22</sup> However, a lower degree of crystallinity decreases the mechanical and thermal properties of CPEs.<sup>23</sup> Therefore, it is necessary to develop a universal approach to increase the  $\text{Li}^+$  transport in CPEs without further increasing the content of amorphous region.

In this study, we propose the strategy of controlling the chain folding structure in the crystalline region to increase the mobility of the chains by adjusting the size of the  $\text{Al}_2\text{O}_3$  nanofiller. Herein, we highlight that the present CPEs with 30 nm  $\text{Al}_2\text{O}_3$  nanofillers (CPEs-30) exhibit an excellent electrochemical performance with a capacity retention of 81.3% after 500 cycles at 1.0C in LFP/CPE/Li batteries, which is better than that CPEs with larger  $\text{Al}_2\text{O}_3$  fillers.

## Results and discussion

The different-sized  $\text{Al}_2\text{O}_3$  powders are shown in Fig. S1.† Also, the CPEs are shown in Fig. S2,† where we found that the  $\text{Al}_2\text{O}_3$  powders were homogeneously dispersed in the polymer matrix. The crystalline morphology of the CPEs was investigated, as shown in Fig. 1(a)–(f). Numerous spherulites with a hexagon can be observed in the optical microscopy photographs, and the size of the spherulites in the CPEs decreased with an increase in the  $\text{Al}_2\text{O}_3$  particle size. Upon the addition of  $\text{Al}_2\text{O}_3$  particles to the polymer matrix, the spherulite size and the fraction of spherulites decreased, indicating that the nanoparticles play a role in the heterogeneous nucleation in the PCL system.<sup>24</sup> It is known that PCL, acting as a polymer matrix material in CPEs such as

PEO and PVDF, is semi-crystalline.<sup>25–27</sup> Its semi-crystalline texture consists of alternating amorphous and crystalline layers with characteristic thicknesses.<sup>28</sup> As is known, crystal nucleation is necessary for the formation of a new crystalline phase. Thus, when the inorganic nanoparticles were added to PCL, they not only reduced the degree of crystallinity, but also inevitably acted as a nucleating agent to change the crystalline process, which may have increased the number of nucleation sites and decreased the average size of the polymer spherulites.<sup>29</sup> Although nanoparticles are beneficial to promote the formation and growth of crystal nuclei and the crystallization speed, the movement of the PCL molecular chains will be restricted, reducing the crystalline region, which can be attributed to the nucleation agent effect.<sup>30</sup> In addition, the 30 nm-sized  $\text{Al}_2\text{O}_3$  nanoparticles inevitably aggregated into clusters with an uneven distribution, which led to an uneven distribution of the polymer crystalline morphology in space. The uneven dispersion and distribution of the fillers in the polymer matrix will weaken the heterogeneous nucleation effect of the inclusions in the matrix. The nano- $\text{Al}_2\text{O}_3$  particles will influence the movement of the PCL molecular chains in this case.<sup>31</sup> Besides, among the nanoparticle-forming clusters, the polymer is amorphous. In the region where the particle clusters are relatively dispersed, there is more free space between the particle clusters, forming a large-size microcrystalline domain, which is generated by the bulk nucleation mechanism. Furthermore, the agglomeration of smaller-sized  $\text{Al}_2\text{O}_3$  particles in CPEs-30 may have reduced the effective nucleation centers, and these big-sized spherulites may have also originated from the assembly of several small spherulites. These results imply that the addition of  $\text{Al}_2\text{O}_3$  particles to PCL may change the degree of chain folding in the polymer matrix. Thus, the crystalline morphology and polymer chain motion may affect the electrochemical performance of the electrolyte.

The  $\sigma$  of the CPEs was determined *via* electrochemical impedance spectroscopy. Fig. 2 shows the  $\sigma$  of the different CPEs. The  $\sigma$  of CPEs-30 was determined to be  $7.63 \times 10^{-6} \text{ S cm}^{-1}$  at  $30^\circ\text{C}$ , which is much more than that of CPEs-100 ( $4.51 \times 10^{-6} \text{ S cm}^{-1}$ ), CPEs-200 ( $2.89 \times 10^{-6} \text{ S cm}^{-1}$ ), and CPEs-400 ( $1.02 \times 10^{-6} \text{ S cm}^{-1}$ ). Specifically,  $\sigma$  increased with rising temperature, as shown in Fig. 2 and Table 1. Clearly, the  $\sigma$  of CPEs-30 is always higher than that of CPEs with larger  $\text{Al}_2\text{O}_3$  particles, and finally reached  $4.87 \times 10^{-5} \text{ S cm}^{-1}$  at  $60^\circ\text{C}$ . The Li-ion transference number ( $t_{\text{Li}^+}$ ), as shown in Fig. 3, is a vital parameter for solid electrolyte, which reflects the transportation of  $\text{Li}^+$  in the CPEs. The  $t_{\text{Li}^+}$  of the CPEs was obtained using eqn (2), where the  $t_{\text{Li}^+}$  value of CPEs-30 is 0.65, while that for CPEs-100, CPEs-200, and CPEs-400 is lower. A larger  $t_{\text{Li}^+}$  is favorable for a higher rate capability and a reduction in the growth of Li dendrites.<sup>32</sup>

Fig. S3(a)–(d)† show the  $\text{Li}^+$  plating/stripping behaviors of CPEs-30, CPEs-100, CPEs-200, and CPEs-400 in symmetric Li cells at a current density in the range of  $0.01$  to  $0.2 \text{ mA cm}^{-2}$  at  $60^\circ\text{C}$ . After 200 h cycles, the over-potential of Li/CPEs-30/Li was stable at about  $90 \text{ mV}$  at  $0.2 \text{ mA cm}^{-2}$ , which indicated the formation of a passivation solid electrolyte interphase (SEI) layer. Furthermore, Li/CPEs-30/Li showed long cycle stability at

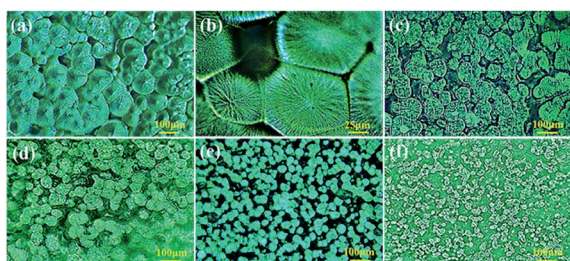


Fig. 1 (a and b) Optical microscope photographs of PCL-LITFSI, (c) CPEs-30, (d) CPEs-100, (e) CPEs-200, and (f) CPEs-400.

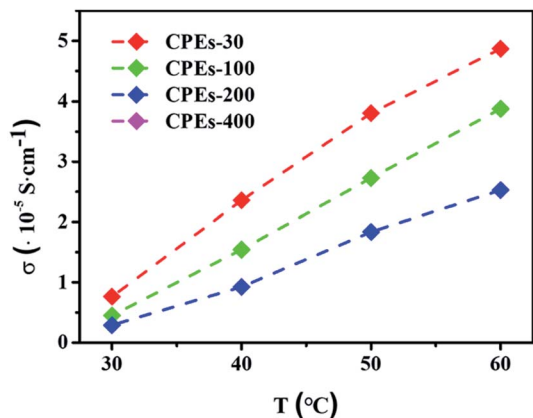


Fig. 2 Li-ion conductivity of CPEs-30, CPEs-100, CPEs-200, and CPEs-400.

Table 1 Conductivity of CPEs-30, CPEs-100, CPEs-200, and CPEs-400 at different temperatures

Sample (S cm <sup>-1</sup> )	30 °C	40 °C	50 °C	60 °C
CPEs-30	$7.63 \times 10^{-6}$	$2.36 \times 10^{-5}$	$3.80 \times 10^{-5}$	$4.87 \times 10^{-5}$
CPEs-100	$4.51 \times 10^{-6}$	$1.54 \times 10^{-5}$	$2.73 \times 10^{-5}$	$3.88 \times 10^{-5}$
CPEs-200	$2.89 \times 10^{-6}$	$9.25 \times 10^{-6}$	$1.84 \times 10^{-5}$	$2.53 \times 10^{-5}$
CPEs-400	$1.02 \times 10^{-6}$	$6.96 \times 10^{-6}$	$1.04 \times 10^{-5}$	$1.72 \times 10^{-5}$

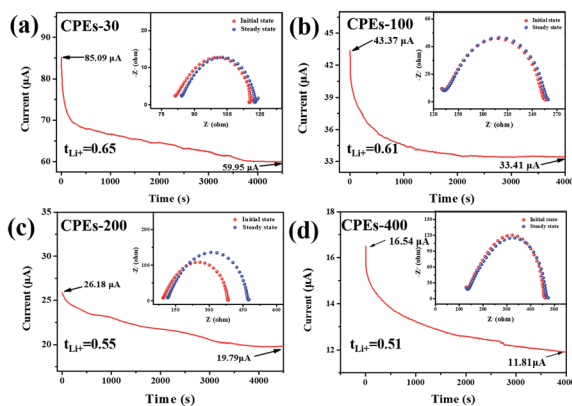


Fig. 3 The transference numbers of (a) CPEs-30, (b) CPEs-100, (c) CPEs-200, and (d) CPEs-400.

the current density of  $0.1 \text{ mA cm}^{-2}$ . As shown in Fig. S3(e),<sup>†</sup> demonstrating the absence of any growth of Li dendrites during the cycling of Li/CPEs-30/Li. However, the symmetric Li cells for CPEs-100 and CPEs-400 showed a short circuit. Although the Li<sup>+</sup> plating/stripping process for Li/CPEs-200/Li was stable, a higher overpotential was obtained for Li/CPEs-200/Li. All these results confirm that CPEs-30 is stable for the Li metal plating/stripping process. The electrochemical stability of the CPE membrane is shown in Fig. S4.<sup>†</sup> These CPEs exhibited a good electrochemical stability window, where their particle size had a low impact on their electrochemical stability. These results show that CPEs-30

exhibited the highest  $\sigma$  and  $t_{\text{Li}^+}$  among the CPEs. We found that the electrochemical performance of CPEs-30 was better than that with larger particles even though the size of the spherulites in CPEs-30 was bigger than that in CPEs-100, CPEs-200, and CPEs-400. These features may result from the looser chain folding in the crystal region of CPEs-30.

To evaluate the performance of the prepared CPEs, LFP/CPEs/Li batteries were assembled and their rate and cycle performance were monitored at  $60^\circ\text{C}$ . As shown in Fig. 4(a), the initial discharge capacity of CPEs-30 was  $129.9 \text{ mA h g}^{-1}$  at  $0.1\text{C}$ . After ten cycles, the capacity increased gradually to  $156.4 \text{ mA h g}^{-1}$  due to the wetting process of the electrode interface by the electrolyte. The rate and charge-discharge performance of the cell, as shown in Fig. 4(a), presented the discharge specific capacities of LFP/CPEs-30/Li with different rates ( $0.1, 0.2, 0.5, 0.8$  and  $1\text{C}$ ) at  $60^\circ\text{C}$ , corresponding to  $156.4, 147.5, 130.7, 117.3$  and  $110.3 \text{ mA h g}^{-1}$ , respectively. Furthermore, the corresponding discharge specific capacities in the LFP/CPEs-100/Li system decreased to  $133.9, 128.0, 118.6, 112.3, 108.1 \text{ mA h g}^{-1}$ ,  $128.0, 124.1, 113.9, 104.0, 97.0 \text{ mA h g}^{-1}$  in the LFP/CPEs-200/Li system, and  $95.5, 89.5, 76.7, 69.8, 65.6 \text{ mA h g}^{-1}$  in the LFP/CPEs-400/Li system, respectively. The capacity reduction of LFP/CPEs/Li with larger  $\text{Al}_2\text{O}_3$  particles may be attributed to its lower  $\sigma$  and  $t_{\text{Li}^+}$ . Furthermore, the cycle performance of the batteries at  $1.0\text{C}$ , as shown in Fig. 4(b), exhibited the good capacity retention of LFP/CPEs-30/Li. The first discharge capacity of the LFP/CPEs-30/Li cell was  $118.2 \text{ mA h g}^{-1}$ , and then it displayed an increasing trend with an increase in cycle number, indicating the slow activation process of the cell. Specifically, a reversible discharge capacity of  $117.2$  and  $96.1 \text{ mA h g}^{-1}$  for the 300th and 500th cycles were achieved, with the capacity retention of  $99.2\%$  and  $81.3\%$ , respectively. It is noteworthy that the present CPEs-30 compares favorably with the previously reported CPES (Table S1<sup>†</sup>) in terms of battery performance. The morphology and structure of CPEs-30 after cycling are shown in Fig. S5.<sup>†</sup> In contrast, the discharge capacity of LFP/CPEs-100/Li, LFP/CPEs-200/Li, and LFP/CPEs-400/Li cells decayed rapidly at the same cycle numbers, as shown in Fig. 4(b). After 500 cycles, the discharge capacity of these cells was only  $64.0\%$ ,  $60.0\%$ , and  $31.7\%$  of their initial capacitance, respectively.

To further verify the change in chain folding and compare the mobility of the polymer chains in the CPEs, the spin-lattice relaxation time ( $T_1$ ) and transverse relaxation time ( $T_2$ ) of CPEs-30 and CPEs-200 were investigated using the saturation-

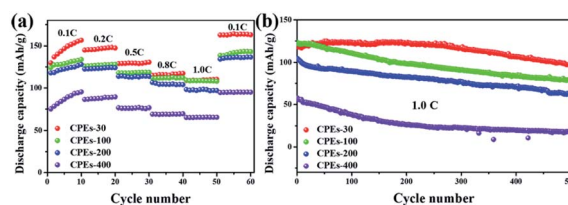


Fig. 4 (a) Rate performance of CPEs-30, CPEs-100, CPEs-200, and CPEs-400 and (b) cycle performance of CPEs-30, CPEs-100, CPEs-200, and CPEs-400 in LiFePO<sub>4</sub>/CPEs/Li battery.

recovery pulse sequence and CPMG (Carr–Purcell–Meiboom–Gill) method *via* solid-state NMR. The relaxation process of  $T_1$  is sensitive to high frequency molecular motions, whereas  $T_2$  is sensitive to low frequency molecular motions (*e.g.*, large amplitude chain wagging).<sup>33</sup> The activity of molecular motion can be determined using the correlation time,  $\tau$ . The slow migration of molecules corresponds to a large  $\tau$ , given that  $T_2$  decreases with an increase in  $\tau$ , as reported by Bloembergen. Therefore,  $T_2$  can be used to reflect the speed of molecular motion. A larger value of  $T_2$  implies faster molecular motion. It should be mentioned that the changes in  $T_1$  are opposite to  $T_2$  for high molecular weight polymers.<sup>34</sup>

Given that spin-lattice relaxation is a process in which the RF energy returns to the ground state during the nuclear spin release excitation, the relationship between the observed signal and time is analyzed using the initial magnetization vector reversed by 180° pulse. The spin-lattice relaxation is sensitive to high frequency motion in macromolecular chains and mainly reflects the high frequency and short-range motion of the chains, revealing the specific nature and influence of nano-fillers on the molecular level dynamics in polymer membranes.<sup>35</sup> The  $T_1$  values are related to the mobility/rigidity of the polymer.<sup>36</sup> It can be observed from Fig. 5(a) that the  $T_1$  of CPEs-30 is 543.9 ms, and it increases to 577.5 ms in CPEs-200, indicating faster migration of molecules in CPEs-30 and smaller local packing density of polymer chains.<sup>37</sup>

$T_2$  is related to the local segmental motion. Also,  $T_2$  reflects the decay rate of transverse magnetization and results from the local dipole magnetic field produced by the adjacent spin nuclei, which depends on the direction and position of the adjacent spin nuclei. The information of the spin-environment coupling and timescale of motion of the environment can be inferred.<sup>38</sup>  $T_2$  is mainly determined by the intensity of the 1H–1H dipole interaction and segmental motion. A greater distance between protons usually leads to faster movement of segments and weak interaction of 1H–1H dipoles, which finally increases  $T_2$ . Romo-Uribe reported that faster the signal intensity decays (short  $T_2$ ), the more restricted the polymer motion,<sup>39</sup> where a longer  $T_2$  corresponds to higher molecular motion.<sup>40</sup> Fig. 5(b) shows the comparison of  $T_2$  between CPEs-30 and CPEs-200. We found that the  $T_2$  of CPEs-30 was 2.669 ms, which decreased to 2.051 ms for CPEs-200. It is noteworthy that the  $T_2$  of CPEs-30 and CPEs-200 is bigger than pure PCL, which is 0.8 ms, as reported by Xu.<sup>41</sup> This indicates that the more flexible PCL chains in CPEs-30 resulted from the change in chain folding looseness due to the addition of nanoparticles. The  $T_2$  of CPEs-30 is higher

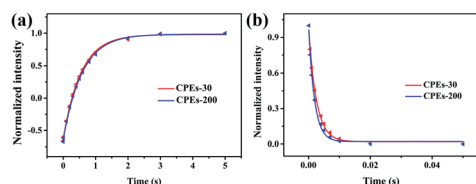


Fig. 5 (a)  $T_1$  fit curves of CPEs-30 and CPEs-200, and (b)  $T_2$  fit curves of CPEs-30 and CPEs-200.

than that of CPEs-200, which reflects the larger distance between the protons of CPEs-30 and the high molecular segmental mobility. Both the tests of  $T_1$  and  $T_2$  are consistent with the assumption based on Fig. 1 that the polymer chains in CPEs-30 possess a looser chain folding structure. This type of loose arrangement of polymer spherulites may promote lithium ion transport and improve the electrochemical performance in CPEs.

Simultaneously, the XRD patterns of pure PCL and CPEs are shown in Fig. S6(a) and (b).† The intensity of the crystalline peaks for PCL was significantly reduced upon the addition of  $\text{Al}_2\text{O}_3$  nanoparticles, which was usually considered to be beneficial for ion transport.<sup>42,43</sup> Fig. S7(a)† shows the TGA test of CPEs-30, CPEs-100, CPEs-200, and CPEs-400. There is a three-stage degradation process for the CPEs. Below 300 °C, the evaporation of water and residual solvents caused the first slight weight loss. The second significant weight loss was due to the decomposition of PCL. Subsequently, the third subsequent degradation was ascribed to the decomposition of LiTFSI. The degradation in pure PCL started from 300 °C to 450 °C, corresponding to the decomposition of PCL. The crystallinity of PCL in CPEs was further studied by differential scanning calorimetry (DSC) measurement, as shown in Fig. S7(b) and Table S2.† The endothermic peak during the heating process corresponds to the melting of the crystallized polymer and an increase in the content of crystallized phase in the polymer matrix would result in an increase in the fusion enthalpy ( $\Delta H_m$ ).<sup>44</sup> It can be seen that the  $\chi_c$  of CPEs-30, CPEs-100, CPEs-200, and CPEs-400 was 40.72%, 41.35%, 45.31%, and 47.00%, respectively, demonstrating that the different-sized  $\text{Al}_2\text{O}_3$  powders did not change the crystallinity of PCL significantly. There was no obvious difference in crystalline degree among CPEs-30, CPEs-100, CPEs-200, and CPEs-400, indicating that the degree of chain folding plays a dominant role in tuning the electrochemical performance of the CPEs.

To better understand the lithium ion transport mechanism in the composite electrolytes, a schematic diagram is presented in Fig. 6. The structure of CPEs is similar to a loose lotus

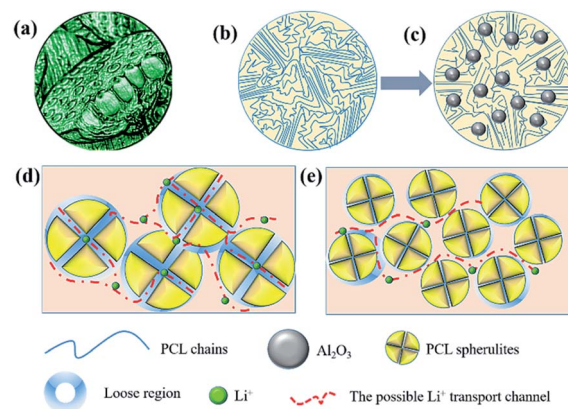


Fig. 6 (a) Structure of lotus seeds, (b) PCL, and (c) CPEs and (d and e) schematic image of the Li ion conducting paths in CPEs-30 and CPEs-200.

seedpod, as shown in Fig. 6(a). Fig. 6(b) and (c) show that when  $\text{Al}_2\text{O}_3$  particles are added to the polymer matrix, the arrangement of polymer chains become more chaotic, corresponding to an increase in  $T_2$  after  $\text{Al}_2\text{O}_3$  particles added compared with pure PCL reported by Xu.<sup>41</sup> More polymer chains can move freely and lithium ions transported quickly in the polymer matrix. In addition, anions as large as  $\text{TFSI}^-$  can be firmly trapped by the PCL chains and  $\text{Al}_2\text{O}_3$  particles, causing them to be immobilized at the interface between the ceramic filler and the polymer matrix, where  $\text{Li}^+$  can freely emerge and move rapidly along the extended interface. Fig. 6(d) and (e) illustrate the  $\text{Li}^+$  transfer path in the PCL matrix. The number of big-sized spherulites in CPEs-30 is less and lithium ions can move a short route in both the amorphous region and the looser region inside the spherulites of PCL to reach the electrode. However, due to the tight stacking of the lamella, the smaller-sized and higher number of spherulites in CPEs-200 block the transport of  $\text{Li}^+$  ions, most probably leading to low conductivity. This result explains the high  $\sigma$  and  $t_{\text{Li}^+}$  of the electrolyte and excellent electrochemical performance of CPEs-30 in the LFP/CPEs/Li battery. The looser chain folding of the crystal region in the polymer provides more lithium ion transport channels and conducting pathways and shorten the path between electrodes, thus improving the electrochemical performance of the electrolytes.<sup>45</sup>

## Experimental

### Synthesis of composite polymer electrolytes

The CPEs were prepared *via* the solution casting method.<sup>46</sup> Appropriate amounts of PCL and LITFSI to give an [O] : [Li] ratio of 20 : 1 were dissolved in dimethyl carbonate, and the solution was stirred at 55 °C for 2 h. A predetermined amount of  $\text{Al}_2\text{O}_3$  powder with different particle sizes was then added, and the solution was mixed for 24 h with continuous heating. When the complete homogenization of the mixture occurred, the solution was cast on a glass plate using a doctor blade. The residual solvent was completely removed by drying the electrolyte film at room temperature for another 24 h. Then the obtained CPE membrane was cut into circular shapes with a diameter of 19 mm and placed in an Ar-filled glove box overnight to remove the residual solvent, and finally for electrochemical tests. Below, PCL-LITFSI- $\text{Al}_2\text{O}_3$ -30 nm, PCL-LITFSI- $\text{Al}_2\text{O}_3$ -100 nm, PCL-LITFSI- $\text{Al}_2\text{O}_3$ -200 nm, and PCL-LITFSI- $\text{Al}_2\text{O}_3$ -400 nm are denoted as CPEs-30, CPEs-100, CPEs-200, and CPEs-400, respectively.

### Battery assembly and electrochemical measurements

Coin cell SS/CPEs/SS (SS, stainless-steel plate electrodes) were assembled to determine the ionic conductivity of the CPEs by alternating current (AC) impedance measurements in the frequency range of 10 MHz to 0.1 Hz with a potential amplitude of 10 mV using a Zahner electrochemical workstation. The ionic conductivity of the composite electrolyte was calculated using eqn (1):<sup>16</sup>

$$\sigma = \frac{L}{RS} \quad (1)$$

where  $L$  is the thickness of the electrolyte membrane,  $R$  represents the impedance of the symmetrical stainless blocking cells, and  $S$  is the electrode area. The coin cell Li/CPEs/SS were assembled to measure the electrochemical window of the CPEs *via* the linear sweep voltammetry (LSV) technique at a scanning rate of 0.1 mV s<sup>-1</sup> using a CHI660E workstation. The Li-ion transference number ( $t_{\text{Li}^+}$ ) was calculated using the Bruce-Vincent formula, as shown in eqn (2):<sup>47</sup>

$$t_{\text{Li}^+} = \frac{I_s(\Delta V - I_0 R_0)}{I_0(\Delta V - I_s R_s)} \quad (2)$$

where  $I_0$  and  $I_s$  represent the initial and stable current obtained from the DC polarization curves of the symmetrical Li/CPEs/Li cell ( $\Delta V = 10$  mV), respectively.  $R_0$  and  $R_s$  correspond to the impedance before and after polarization, respectively. The galvanostatic test of both the Li/CPEs/Li cells and  $\text{LiFePO}_4$ /CPEs/Li full solid-state cells was carried out on a Land battery testing system at 60 °C.

### Relaxation time test

The spin-lattice relaxation time ( $T_1$ ) and transverse relaxation time ( $T_2$ ) were tested *via* solid-state nuclear magnetic resonance (SSNMR) on a Varian VNMRS 700 MHz Nuclear magnetic resonance spectrometer.  $T_1$  and  $T_2$  were calculated using the inversion recovery method and CPMG (Carr–Purcell–Meiboom–Gill) method with eqn (3) and (4), respectively:<sup>48</sup>

$$M = M_0 \left[ 1 - 2 \exp\left(-\frac{t}{T_1}\right) \right] \quad (3)$$

$$M = M_0 \exp\left(-\frac{t}{T_2}\right) \quad (4)$$

where  $M$  is the magnetization vector and  $M_0$  is the initial magnetization vector.

### Materials characterization

XRD patterns were obtained on a D8-ADVANCE X-ray diffractometer using Cu K $\alpha$  radiation. To investigate the thermal degradation behavior of the electrolyte membrane, thermogravimetric (TG) analysis was carried out on an STA 449 F3 Thermal Analyzer from room temperature to 900 °C at a heating rate of 10 °C min<sup>-1</sup>. The glass transition temperature and crystallinity of PCL were measured *via* differential scanning calorimetry (DSC) between -80 °C and 180 °C. The crystallinity of CPEs ( $\chi_c$ ) was calculated using eqn (5):<sup>49</sup>

$$\chi_c = \left( \frac{\Delta H_m}{\Delta H_0} \times (1 - \varphi_{\text{add}}) \right) \times 100\% \quad (5)$$

where  $\Delta H_m$  is the fusion enthalpy of the sample and  $\Delta H_0$  (139.3 J g<sup>-1</sup>)<sup>50</sup> is the fusion enthalpy of 100% crystallized PCL, and  $\varphi_{\text{add}}$  is the total weight percentage of additives.

## Conclusions

In summary, four types of CPEs were fabricated by introducing different-sized  $\text{Al}_2\text{O}_3$  nanoparticles in the PCL polymer matrix.

The CPEs with smaller-sized Al<sub>2</sub>O<sub>3</sub> exhibited a larger  $T_1$  and smaller  $T_2$ , implying the looser chain folding structure of CPEs-30, which has a crucial effect on the ion transport behaviors. Moreover, the LFP/CPEs-30/Li battery delivered a reversible capacity of 156.4 mA h g<sup>-1</sup> and showed a high capacity retention of 81.3% after 500 cycles at 1.0C. We highlighted that the looser chain folding structure can provide more transport channels and conducting pathways for the transportation of Li-ions, which can ultimately facilitate the development of design principles for future high-performance CPEs.

## Author contributions

Hongyun Jin and Rui Ma conceived the project. Dexuan Pei conducted the synthesis of materials, characterizations, and electrochemical tests. Gang Yan helped pre-process some materials. Yuhang Li and Can Huang helped to measure samples and to analyze the data. Ziyang Liu helped take SEM pictures. Dexuan Pei wrote the paper, and Shuo Huang helped polish this manuscript. All the authors discussed the results and commented on the manuscript.

## Conflicts of interest

There are no conflicts to declare.

## Acknowledgements

This work was financially supported by the National Natural Science Foundation of China (12192213), the Key Research and Development Program of Hubei (2021BAA175), and the National Key Research and Development Program of China (2019YFA0708401). The authors thank Professor Liying Wang of National Center for Magnetic Resonance in Wuhan Innovation Academy for Precision Measurement Science and Technology, Chinese Academy of Sciences, for her help with the solid state NMR measurements.

## References

- P. Fan, H. Liu, V. Marosz, N. T. Samuels, S. L. Suib, L. Sun and L. Liao, *Adv. Funct. Mater.*, 2021, **31**, 2101380.
- F. Duffner, N. Kronemeyer, J. Tübke, J. Leker, M. Winter and R. Schmich, *Nat. Energy*, 2021, **6**, 123–134.
- K. Fu, Y. Gong, B. Liu, Y. Zhu, S. Xu, Y. Yao, W. Luo, C. Wang, S. Lacey, J. Dai, Y. Chen, Y. Mo, E. Wachsman and L. J. S. A. Hu, *Sci. Adv.*, 2017, **3**, e160165.
- A. Paoletta, W. Zhu, G. L. Xu, A. La Monaca, S. Savoie, G. Girard, A. Vijn, H. Demers, A. Perea, N. Delaporte, A. Guerfi, X. Liu, Y. Ren, C. J. Sun, J. Lu, K. Amine and K. Zaghbi, *Adv. Energy Mater.*, 2020, **10**, 2001497.
- O. Sheng, C. Jin, X. Ding, T. Liu, Y. Wan, Y. Liu, J. Nai, Y. Wang, C. Liu and X. Tao, *Adv. Funct. Mater.*, 2021, **31**, 2100891.
- X. Chen, W. He, L. X. Ding, S. Wang and H. Wang, *Energy Environ. Sci.*, 2019, **12**, 938–944.
- H. Yang, J. Bright, B. Chen, P. Zheng, X. Gao, B. Liu, S. Kasani, X. Zhang and N. Wu, *J. Mater. Chem. A*, 2020, **8**, 7261–7272.
- D. E. Fenton, J. M. Parker and P. V. Wright, *Polymer*, 1973, **14**, 589.
- M. Armand, *Solid State Ionics*, 1983, **9–10**, 745–754.
- K. Liu, M. Wu, H. Jiang, Y. Lin and T. Zhao, *J. Mater. Chem. A*, 2020, **8**, 18802–18809.
- C. C. Sun, A. H. You and L. L. Teo, *J. Polym. Eng.*, 2019, **39**, 612–619.
- G. B. Berhe, W. N. Su, L. H. Abrha, H. K. Bezabh, T. M. Hagos, T. T. Hagos, C. J. Huang, N. A. Sahalie, B. A. Jote, B. Thirumalraj, D. Kurniawan, C. H. Wang and B. J. Hwang, *J. Mater. Chem. A*, 2020, **8**, 14043–14053.
- S. Xu, Z. Sun, C. Sun, F. Li, K. Chen, Z. Zhang, G. Hou, H. M. Cheng and F. Li, *Adv. Funct. Mater.*, 2020, **30**, 2007172.
- Q. Cheng, A. Li, N. Li, S. Li, A. Zangiabadi, T. D. Li, W. Huang, A. C. Li, T. Jin, Q. Song, W. Xu, N. Ni, H. Zhai, M. Dontigny, K. Zaghbi, X. Chuan, D. Su, K. Yan and Y. Yang, *Joule*, 2019, **3**, 1510–1522.
- Z. Lu, Z. Yang, C. Li, K. Wang, J. Han, P. Tong, G. Li, B. S. Vishnugopi, P. P. Mukherjee, C. Yang and W. Li, *Adv. Energy Mater.*, 2021, **11**, 2003811.
- Y. Nikodimos, L. H. Abrha, H. H. Weldeyohannes, K. N. Shitaw, N. T. Temesgen, B. W. Olbasa, C. J. Huang, S. K. Jiang, C. H. Wang, H. S. Sheu, S. H. Wu, W. N. Su, C. C. Yang and B. J. Hwang, *J. Mater. Chem. A*, 2020, **8**, 26055–26065.
- W. Zhang, J. Nie, F. Li, Z. L. Wang and C. Sun, *Nano Energy*, 2018, **45**, 413–419.
- F. Chen, W. Zha, D. Yang, S. Cao, Q. Shen, L. Zhang and D. R. Sadoway, *J. Electrochem. Soc.*, 2018, **165**, A3558–A3565.
- Y. W. Chen Yang, H. C. Chen, F. J. Lin and C. C. Chen, *Solid State Ionics*, 2002, **150**, 327–335.
- L. Zhang, S. Wang, J. Li, X. Liu, P. Chen, T. Zhao and L. Zhang, *J. Mater. Chem. A*, 2019, **7**, 6801–6808.
- C. Sun, J. Liu, Y. Gong, D. Wilkinson and J. Zhang, *Nano Energy*, 2017, **33**, 363–386.
- J. Zheng and Y. Y. Hu, *ACS Appl. Mater. Interfaces*, 2018, **10**, 4113–4120.
- D. Lin, P. Y. Yuen, Y. Liu, W. Liu, N. Liu, R. H. Dauskardt and Y. Cui, *Adv. Mater.*, 2018, **30**, 1802661.
- J. Mikešová, M. Šlouf, U. Gohs, D. Popelková, T. Vacková, N. H. Vu, J. Kratochvíl and A. Zhigunov, *Polym. Bull.*, 2014, **71**, 795–818.
- R. J. Sengwa and P. Dhatwarwal, *Electrochim. Acta*, 2020, **338**, 135890.
- X. N. Wen, Y. L. Su, G. M. Liu, S. F. Li, A. J. Muller, S. K. Kumar and D. J. Wang, *Macromolecules*, 2021, **54**, 1870–1880.
- M. M. Machado Paula, M. A. F. Corat, M. Lancellotti, G. Mi, F. R. Marciano, M. L. Vega, A. A. Hidalgo, T. J. Webster and A. O. Lobo, *Mater. Sci. Eng., C*, 2020, **111**, 110706.
- W. Hu, *Phys. Rep.*, 2018, **747**, 1–50.
- M. Slouf, S. Krejčíková, T. Vacková, J. Kratochvíl and L. Novak, *Front. Mater.*, 2015, **2**, 23.

- 30 J. Z. Liang, L. Zhou, C. Y. Tang and C. P. Tsui, *Composites, Part B*, 2013, **45**, 1646–1650.
- 31 J. Z. Liang, *Polym. Int.*, 2012, **61**, 511–515.
- 32 W. Zha, F. Chen, D. Yang, Q. Shen and L. Zhang, *J. Power Sources*, 2018, **397**, 87–94.
- 33 A. J. Deese, E. A. Dratz, L. Hymel and S. Fleischer, *Biophys. J.*, 1982, **37**, 207–216.
- 34 N. Bloembergen and L. Morgan, *J. Chem. Phys.*, 1961, **34**, 842–850.
- 35 F. Begni, G. Paul, E. Lasseguette, E. Mangano, C. Bisio, M. C. Ferrari and G. Gatti, *ACS Appl. Polym. Mater.*, 2020, **2**, 3481–3490.
- 36 A. J. Hill, S. J. Pas, T. J. Bastow, M. I. Burgar, K. Nagai, L. G. Toy and B. D. Freeman, *J. Membr. Sci.*, 2004, **243**, 37–44.
- 37 C. H. Lau, P. T. Nguyen, M. R. Hill, A. W. Thornton, K. Konstas, C. M. Doherty, R. J. Mulder, L. Bourgeois, A. C. Y. Liu, D. J. Sprouster, J. P. Sullivan, T. J. Bastow, A. J. Hill, D. L. Gin and R. D. Noble, *Angew. Chem., Int. Ed.*, 2014, **53**, 5322–5326.
- 38 R. Bhattacharyya, I. Chakraborty, A. Chakrabarti and S. Mandal, in *Annual Reports on NMR Spectroscopy*, ed. G. A. Webb, Academic Press, 2020, vol. 99, pp. 57–77.
- 39 A. Romo-Uribe, *Polym. Adv. Technol.*, 2021, **32**, 3082.
- 40 H. Yoshizawa, A. Takazawa, M. Kakiage, T. Yamanobe, N. Hayashi, M. Hiraoka, H. Masunaga, K. Aoyama and H. Uehara, *Sens. Actuators, A*, 2021, **323**, 112634.
- 41 L. F. Hou, H. L. Huang, Z. L. Yang and M. Xu, *J. Funct. Polym.*, 2018, 585–594.
- 42 K. K. Wimalaweera, V. A. Seneviratne and M. A. K. L. Dissanayake, *Procedia Eng.*, 2017, **215**, 109–114.
- 43 X. Zhang, T. Liu, S. Zhang, X. Huang, B. Xu, Y. Lin, B. Xu, L. Li, C. W. Nan and Y. Shen, *J. Am. Chem. Soc.*, 2017, **139**, 13779–13785.
- 44 M. R. Johan, O. H. Shy, S. Ibrahim, S. M. Mohd Yassin and T. Y. Hui, *Solid State Ionics*, 2011, **196**, 41–47.
- 45 M. Forsyth, S. Jiazeng and D. R. MacFarlane, *Electrochim. Acta*, 2000, **45**, 1249–1254.
- 46 X. Li, D. Wang, H. Wang, H. Yan, Z. Gong and Y. Yang, *ACS Appl. Mater. Interfaces*, 2019, **11**, 22745–22753.
- 47 D. Cai, D. Wang, Y. Chen, S. Zhang, X. Wang, X. Xia and J. Tu, *Chem. Eng. J.*, 2020, **394**, 124993.
- 48 S. Meiboom, *Rev. Sci. Instrum.*, 1958, **29**, 688–691.
- 49 T. Eriksson, J. Mindemark, M. Yue and D. Brandell, *Electrochim. Acta*, 2019, **300**, 489–496.
- 50 M. J. Jenkins and K. L. Harrison, *Polym. Adv. Technol.*, 2006, **17**, 474–478.